Feasibility Study of Embedded Wind Energy Harvesting System for Parafoil-Payload Aircraft

Matthew Dowling* and Mark Costello†
Georgia Institute of Technology, Atlanta, Georgia 30332

A logistics issue for guided air-drop systems is maintaining batteries inside the airborne guidance unit so that when the system is deployed the batteries are adequately charged to power onboard electronics and actuators. It is typical for a guided air-drop system to be packed and readied for use well before deployment, leading to nonnegligible battery self-discharge. This necessitates a process to both monitor battery life and recharge the systems after a certain time interval. This paper explores, using a small-scale wind turbine system, providing the requisite power for onboard electronics and actuation for a guided air-drop system. Sizing studies are reported to estimate the necessary size of the rotor and generator. Using this information, a full-scale airborne guidance unit was designed, fabricated, and tested in a wind tunnel. Results indicate that a 0.33 m diam turbine system can generate over 3.7 W of continuous power, which is sufficient to provide power to low-power consumption guided air-drop systems, such as a bleed-air actuated system.

Nomenclature

A	=	rotor cross-sectional area, m²
a	=	axial induction factor
a'	=	angular induction factor
C_p	=	power coefficient
K_t	=	motor torque constant, $(N \cdot m)/A$
P_W	=	power in wind, W
Q	=	total torque generated by rotor, $N \cdot m$
α	=	angle of attack, rad
λ	=	tip-speed ratio
ρ	=	density of air, kg/m³

I. Introduction

GUIDED air-drop systems offer an efficient means of accurately and consistently delivering payloads to remote or hard-to-access locations. A typical guided air-drop system consists of three major components: the parafoil, the payload, and the airborne guidance unit (AGU) (Fig. 1) [1]. The AGU is the component that separates a guided air-drop system from its unguided counterpart, serving to house the sensors, actuators, microprocessors, and batteries responsible for controlling the system. Guided air-drop systems make use of sensors such as GPS, accelerometers, gyroscopes, magnetometers, and barometers to drive the actuators that steer the system. The integration of these sensors and their control mechanisms has greatly enhanced the landing accuracy of parafoil-payload aircraft.

In a practical setting, guided air-drop systems are packed and readied for flight well in advance of their use. During the time between packing and deployment, batteries inside the AGU self-discharge at a nominal rate. For example, the typical self-discharge rates of common rechargeable battery cells are as follows: nickel–cadmium (15–20% per month), nickel metal hydride (20–30% per month), and lithium (5–10% per month) [2]. If the guided air-drop system is unattended for too long a period after packing, the batteries can lose their charge,

resulting in possible failure of the AGU and the flight. Thus, these systems must be monitored and maintained at regular intervals to ensure batteries have the necessary charge for proper operation. This represents an unwanted logistics and maintenance burden for soldiers.

An alternative to powering guided air-drop systems with batteries is to use an onboard, small-scale wind-energy-harvesting system. There is a myriad of ways to harness wind energy on a small scale such as vertical and horizontal axis wind turbines, aerodynamic flutter, vortex-induced vibrations, and galloping [3–7]. While many industries and researchers have examined different methods of harnessing wind energy, by far the most common and efficient device is the horizontal axis wind turbine (HAWT). Federspiel and Chen [8] used a windmill to supply an air-powered sensor using a commercially available fan blade as a rotor and a low-speed, three-phase, brushless dc servomotor as a generator. They rectified the ac using a three-phase bridge constructed from six diodes and achieved efficiency levels of less than 10% while creating 7–28 mW in 2.5 m/s winds and a resistive load of 100 Ω. Rancourt et al. [9] evaluated a microwindmill with a diameter of 4.2 cm and achieved efficiency levels of 1.5% at a wind speed of 5.5 m/s and 9.5% at 11.8 m/s. The generated power varied between 2.4 and 130 mW, respectively. For powering wireless sensors, Xu et al. [10] used a miniature wind turbine consisting of a 7.6 cm plastic propeller blade as a rotor and a permanent magnet dc motor as a generator. With wind speeds of 4.5 m/s, they generated 18 mW of power at an efficiency of 7.6%. An overview of the results from similar small-scale HAWTs is provided in Table 1 [11–16].

As shown in Fig. 2, Danick et al. [17] performed an analysis comparing the efficiency of several small-scale wind-energy devices, plotting efficiencies vs wind speed: solid marks indicate wind turbines, open marks indicate vortex shedding devices, and hash marks indicate flutter/galloping devices. It is clear that no current small-scale wind-energy-harvesting systems approach the theoretical Betz limit of 59.3% and that small-scale turbines typically have a much higher overall efficiency than other mechanisms.

For a parafoil canopy to be properly inflated, guided air-drop systems must fly through the atmosphere at a certain minimum airspeed. Depending on a number of factors, such as the weight of the overall system and the canopy area, lightweight guided air-drop systems have an airspeed in the range of 6–13 m/s. Thus, a guided air-drop system has access to a 6–13 m/s wind stream during the entirety of its flight. A HAWT immersed in such a wind field can extract a percentage of this wind energy.

It is well known that the maximum power extraction potential of an ideal rotor in a wind stream behaves according to

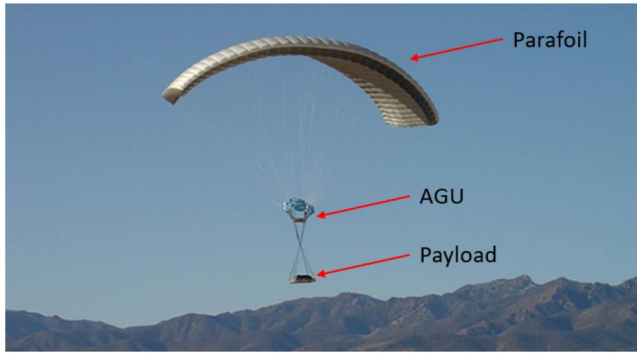$$P_W = \frac{1}{2}\rho A U_1^3 C_P \qquad (1)$$

Fig. 1   Dragonfly guided air-drop system [1].

In the equation, ρ is the density of the air, A is the cross-sectional area of the rotor, U_1 is the relative wind speed, and C_P is the coefficient of power. The theoretical limit of C_P, the Betz limit, is 0.593 and represents the maximum possible power that can be extracted from the wind by a rotor [18]. While power coefficient levels of modern wind turbines have been trending toward this limit, only large-scale systems typically achieve a power coefficient of over 50%. At smaller scales, power coefficients usually drop dramatically due to the aerodynamic characteristics of airfoils at low Reynolds numbers. In addition, gear boxes typically have lower efficiencies at very small scales and can decrease the efficiency further by as much as 50%. Nevertheless, a significant amount of power can be harnessed from a relatively small HAWT rotor radius for the range of wind speeds experienced by guided air-drop systems (Fig. 3).

The paper begins by describing an analysis method to design a HAWT system for a guided air-drop application. This is followed by a detailed description of the newly designed AGU with two HAWTs integrated in the AGU structure. Finally, power extraction results from wind tunnel tests are presented for the designed system at different wind speeds, configurations, and orientations.

II.   Wind Turbine-Generator Optimization

In its simplest form, a wind turbine is composed of four main components: the rotor, the gear box, a generator mechanism, and an electrical load. A flow chart of the interactions between components is shown in Fig. 4.

To harness the maximum possible energy using a wind turbine, the operating point of the aerodynamics subsystem, consisting of the rotor, and the electrical subsystem, composed of the generator and electrical load, must be matched to optimize system performance. Ideally, the system would operate at each subsystem's most efficient point. However, because of the complex coupled dynamics between the subsystems, this is not always possible. Given any three components, the fourth component can be varied to determine a local maximum efficiency. For instance, for a selected rotor, gear box, and generator, the electrical load can be varied to find the maximum efficiency of this configuration.

To facilitate the design of the wind-energy-harvesting mechanism, an initial analysis will be conducted to determine the most efficient operating point of each individual subsystem. Then, these analysis techniques will be applied to candidate rotors and generators to aid in selecting the appropriate rotor and generator for the energy-harvesting application.

Bleed-air actuation represents a low-power means to control a guided air-drop system. It consists of a set of small electric motor actuators embedded inside the parafoil canopy that open holes in the upper surface to create changes in aerodynamic loads [19]. Power consumption for a set of four bleed-air actuators during a typical flight is shown in Fig. 5 and is used to define system energy requirements. Integrating power consumption for all the actuators provides an energy requirement of 12 mA · h (with a nominal voltage of 8 V). Power consumption from the sensors is considered negligible. An air-drop integrated wind-energy system that extracts 3 W of power provides 23 mA · h of energy, exceeding energy needs of the bleed-air actuator system.

A.   Aerodynamic Analysis

The Betz limit analysis, described by Eq. (1), is the maximum possible power that can be extracted from the wind using a HAWT. Practically, aerodynamic inefficiencies such as the wake rotation, nonideal rotor geometry, and tip losses decrease the amount of power a turbine can extract. A variant of the blade element momentum theory method presented by Manwell et al. [20] was used to analyze the behavior of a selected rotor. Refer to [20] for a step-by-step iterative solver for simulating wind turbine aerodynamics at a single wind speed for a desired tip-speed ratio. For this analysis, the blade element momentum theory procedure presented in [20] was modified to include measured geometry (chord and twist distributions) of candidate systems rather than optimally determining the geometry.

The solver operates by iterating on the axial and angular induction factors, a and a', for each blade element. These parameters are defined by Eqs. (2) and (3), in which U_2 is the wind velocity at the rotor plane, ω is the rotational velocity imparted to the flow stream, and Ω is the angular velocity of the rotor. Using an optimum rotor analysis as an initial estimate for a and a' and knowledge of the airfoil's chord, twist, and lift and drag characteristics, an updated value for a and a' can be calculated for each blade element. This process continues until specified conditions are met; namely, the difference between iterations of the axial induction factor is within a specified tolerance, and the value of the parameters have physical significance:

$$a = \frac{U_1 - U_2}{U_1} \qquad (2)$$

$$a' = \frac{\omega}{2\Omega} \qquad (3)$$

An important parameter in blade element momentum theory analysis is the tip-speed ratio of a rotor. The tip-speed ratio is defined by Eq. (4), in which R is the radius of the rotor, Ω is the hub angular velocity, and U_1 is the freestream velocity. This analysis repeats the procedure in [20] for several wind speeds at varying tip-speed ratios to determine the effect of wind speed and tip-speed ratio on power production,

$$\lambda = \frac{\Omega R}{U_1} \qquad (4)$$

Table 1   Small-scale wind turbine examples

| Authors	No. blades	Rotor Diameter, cm	Air speed, m/s	Maximum power, mW	Maximum efficiency, %	Power density, mW/cm²
Federspiel and Chen [8]	4	10	2.5	8	10	0.10
Holmes et al. [11]	24	0.75	40	1.1	0.4	2.26
Hirahara et al. [12]	4	50	9.4	2965	28	1.51
Priya et al. [13]	12	10.2	4.4	5	1.1	0.06
Rancourt et al. [9]	3	4.2	11.8	130	9.5	9.39
Myers et al. [14]	——	12.7 (3×)	4.5	5	——	——
Xu et al. [10]	4	7.6	4.5	18	7.6	0.4
Carli et al. [15]	4	6.3	4.4	10	——	0.32
Sardini et al. [16]	2	6.5	9	45	13–15	1.36
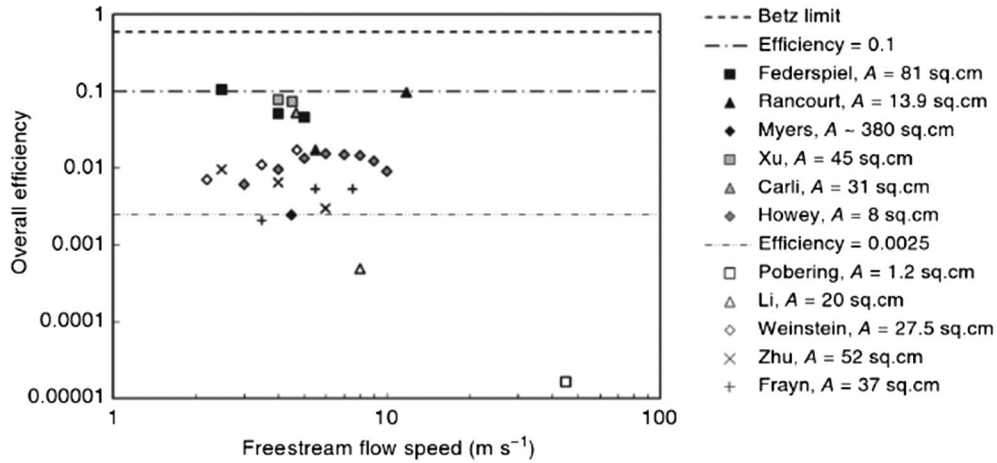
Fig. 2   Efficiency vs wind speed for a variety of micro-wind-energy-harvesting devices [17].
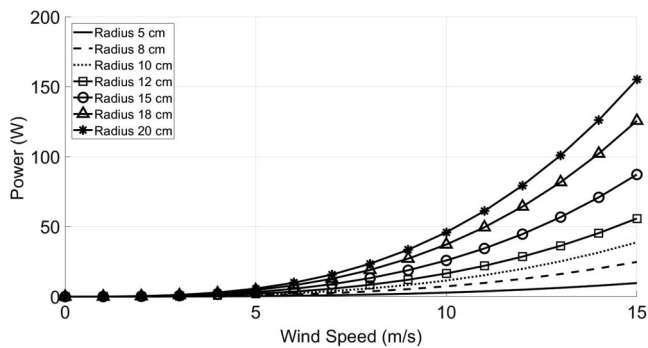

Fig. 3   Extractable power using a wind turbine operating at the Betz efficiency vs wind speed for varying cross-sectional area radii.

B.   Generator Analysis

When using a permanent magnet dc generator, two main factors influence the efficiency of the system: the angular velocity of the generator and the load impedance. The angular velocity of the generator can in part be controlled via a gear box to obtain the specific motor's optimum angular velocity. Ideally, the maximum power transfer of a dc generator occurs when the output impedance of the electrical load matches the internal impedance of the generator. At a steady state, the impedance of the generator is simply the resistance of the internal windings.

To determine the efficiency of a specific generator, an experiment in which a dc motor can be used to drive the generator can be devised. The efficiency of the generator can be determined with knowledge of the stall torque and no-load speed of the driving motor and by measuring the voltage into the motor, the angular velocity of the motor, and the voltage out of the generator.

To calculate the output power of the dc motor, thus the power into the generator, Eqs. (5–7) can be used to first calculate the torque. These equations arise from analyzing a linear approximation of a torque vs speed curve. In Eqs. (5–7), K_t^2/R and K_t/R are constants specific to the selected motor, τ_s is the stall torque, ω_0 is the no-load speed, V is the voltage driving the motor, and ω is the angular velocity of the motor,
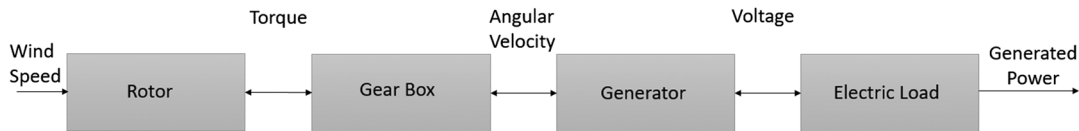
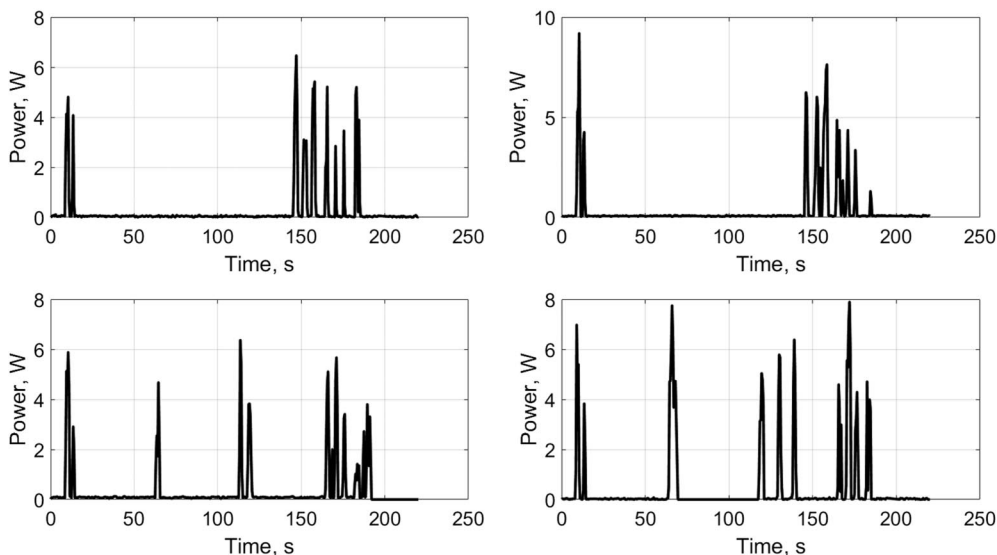

Fig. 4   Subsystem flow chart.

Fig. 5   Power recorded from a bleed-air actuated flight for each actuator.

$$\frac{K_t^2}{R} = \frac{\tau_s}{\omega_0} \qquad (5)$$

$$\tau_s = \frac{K_t}{R} V \qquad (6)$$

$$\tau = \frac{K_t}{R} V - \frac{K_t^2}{R} \omega \qquad (7)$$

Once the torque has been calculated, the power output of the motor is given by

$$P = \tau \omega \qquad (8)$$

Using encoder measurements to determine angular velocity and measuring the voltage being supplied to the dc motor, the power input to the generator can be determined. The torque from the first motor is used to drive the generator to its steady-state angular velocity. Once the steady-state value is reached, the power output of the generator can be determined by measuring the generated voltage drop across a known resistor. This analysis can be conducted at a variety of generator angular velocities and output resistance values to determine the optimal combination of rotational speed and output impedance.

C. Example Analysis

To achieve the optimal efficiency of the system, the operating points of the aerodynamic and electrical subsystems must be matched properly. To highlight the generator–rotor matching process, an example rotor and generator are considered using the analysis methods described previously. The candidate rotor has three blades and a diameter of 0.33 m. The blades have a pitch of 0.15 m and employ a Clark-Y airfoil section. The chord distribution can be found in Table 2 and was determined by dividing the blade into nine elements and taking measurements at the midpoint of each element. This division can be more clearly seen in Fig. 6. The coefficients of lift and drag were calculated by aggregating data tables from an Xfoil solver for low angles of attack and data for the NACA 0015 at low Reynolds numbers for higher angles of attack [21]. This was deemed acceptable as typical rotors operate well below their stall point. This was verified in simulation.

Figures 7 and 8 show the effect of varying the tip speed and wind velocity on the coefficient of power and the output torque for the selected rotor using the logic described in Sec. II.A. For a given tip-speed ratio, the power and torque generated increase as the wind speed increases, while the coefficient of power remains independent of the wind speed. In addition, there is a clear maximum for the coefficient of power at a tip-speed ratio of approximately 3.75. This will be the desired design point when matching the wind turbine and generator subsystems. It is also worth noting that, while the aerodynamic efficiency is less than the Betz limit prediction, the wind turbine is still able to produce an appreciable amount of power. The power output for a tip-speed ratio of 3.75 at 5 m/s is 2.5 W and at 9 m/s is 15 W.

Table 2 Chord distribution of the selected rotor (r/R, fraction of rotor radius)

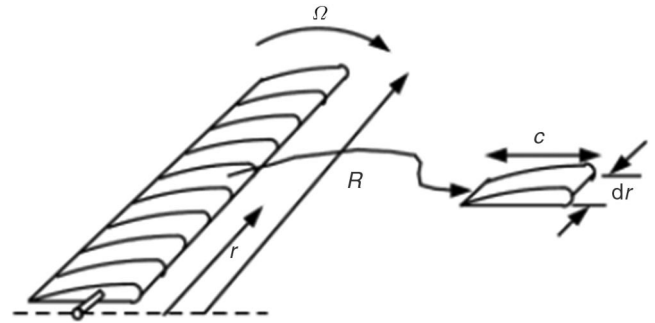| r/R	Chord, m
0.15	0.0239
0.25	0.0231
0.35	0.0235
0.45	0.0245
0.55	0.0249
0.65	0.0241
0.75	0.0240
0.85	0.0203
0.95	0.0178

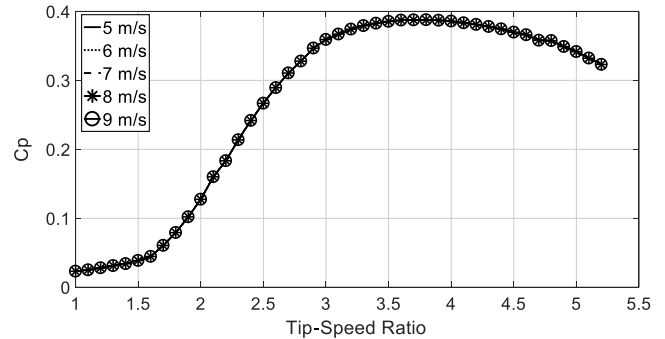**Fig. 6 Rotor blade geometry diagram [20].**

Fig. 7 Coefficient of power vs tip-speed ratio for the Clark-Y airfoil from blade element momentum theory.
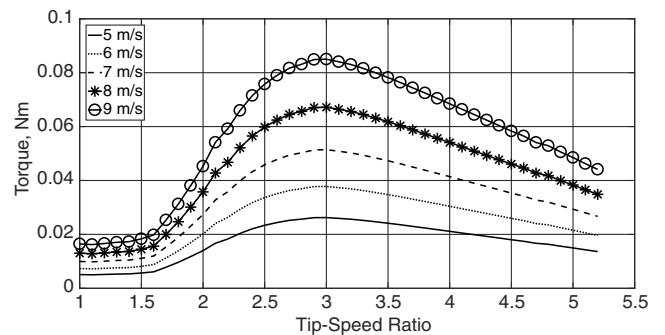

Fig. 8 Torque vs tip-speed ratio for the Clark-Y airfoil from blade element momentum theory.

The candidate generator is a Pololu 25 mm diam medium power gear motor with a 4:1 gear box. The efficiency of the generator was determined experimentally. Each motor was integrated with a 48 count per revolution (CPR) quadrature encoder. A microcontroller was used to convert the encoder readings of the motor shaft to angular velocity. The motor specifications list the stall torque and the no-load speed for the nominal voltage, 12 V. With these two values, the torque-speed curve of the specific motor for any voltage can be approximated linearly by Eq. (7). Thus, the power can be approximated using Eq. (8) (Fig. 9).

To measure the output power of the generator, a simple resistive circuit was created. The voltage drop across the resistor was measured every second for 1 min using a moving average filter. The 60 measurements were then averaged to calculate the nominal voltage. The power output from the generator can be calculated by

$$P_{\text{out}} = \frac{V^2}{R} \qquad (9)$$

The efficiency of the motor can then be determined:

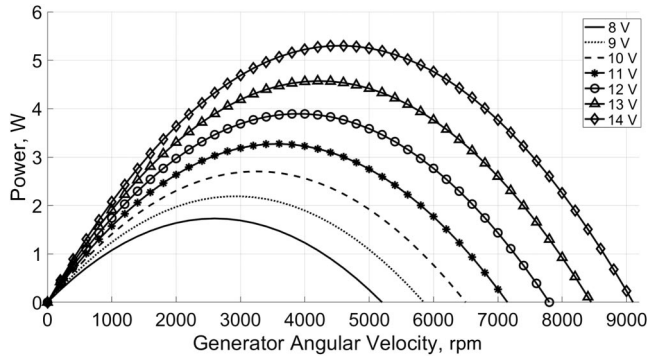$$\eta = 100 \frac{P_{\text{out}}}{P_{\text{in}}} \qquad (10)$$

Fig. 9 Power vs generator angular velocity curve for the Pololu 25 mm diam gear motor.
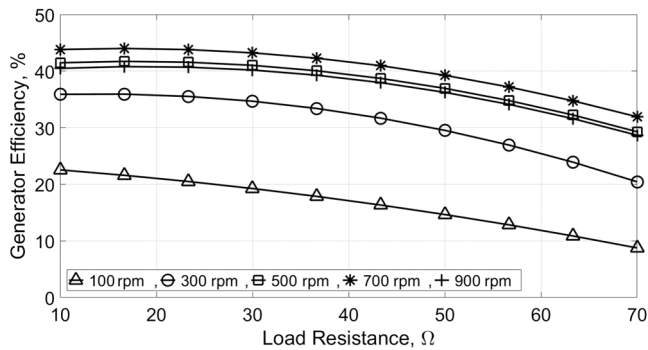

Fig. 10 Second-order polynomial fit for generator efficiency vs load resistance for multiple angular velocities.

The efficiency of the motor was measured for resistance values of 10, 20, 30, 40, 50, 60, and 70 Ω at 100, 300, 500, 700, 900, and 1100 rpm (gear shaft velocity with a 4:1 gear ratio). The motor operated at its highest efficiency for a resistance value of 20 Ω (Fig. 10). The motor's efficiency increased with speed up to 700 rpm and then began to diminish. From Fig. 10, it is evident that the generator's efficiency was a function of both load resistance and angular velocity.

III. Energy-Harvesting System

The AGU design incorporates a wind-energy-harvesting mechanism in a compact housing that protects the wind turbine and includes space for all current AGU functionality such as electronics and avionics. The system provides sufficient power for a low-power consumption guided air-drop system such as a bleed-air actuated system while roughly maintaining the size of current AGUs; the new system is 32.5 in. wide × 17.5 in. tall × 7 in. thick and weighs approximately 10 lbs.

The design is composed of two major subassemblies: the turbine system and the housing. The turbine system is responsible for generating the power required by the onboard electronics and actuators. The housing has three major functions: to hold all onboard electronics and actuators, to protect these components in the event of a high-impact landing, and to act as an attachment point to the parafoil and the payload. The full AGU system can be seen in Fig. 11.

The turbine system, shown in detail in the following, consisted of a propeller, a permanent magnet dc machine to act as a generator, a gear box, a motor mount, and a shaft coupler (Fig. 12). The propeller was selected based on the analysis of multiple commercially available rotor geometries using the blade element momentum theory procedure presented in Sec. II.A. The smallest rotor diameter predicted to produce sufficient power to power a low-power-consumption guided air-drop system, assuming a generator efficiency of approximately 40% based on the analysis from Sec. II.B, was selected.

Two medium-power Pololu 25 mm diam gear motors were used as generators. This motor was selected as it had desirable character-istics, such as a low startup torque and compactness. Moreover,
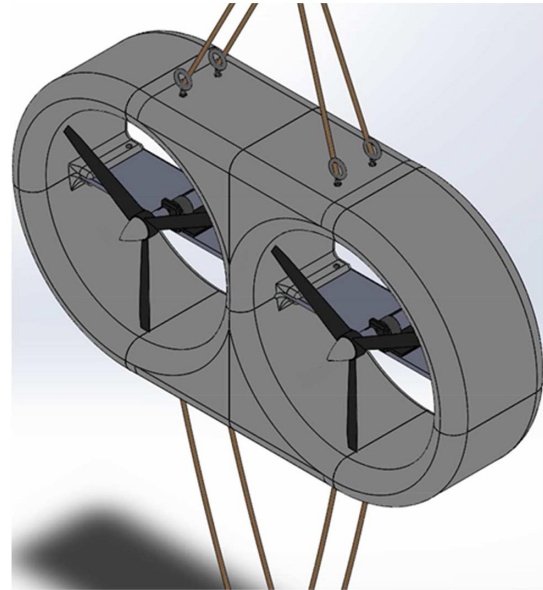

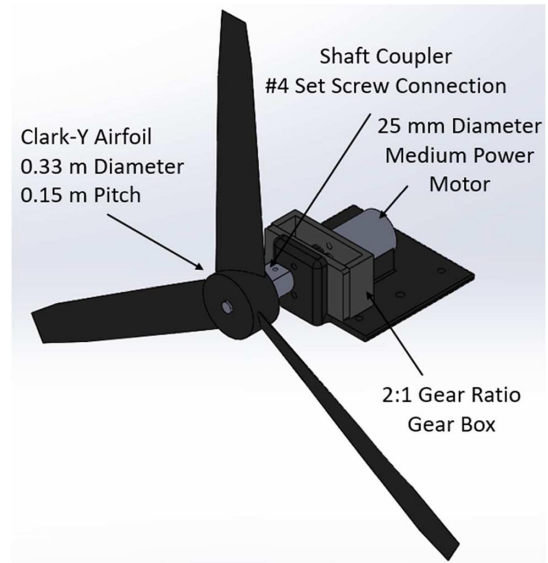**Fig. 11 Self-powered AGU system.**

Fig. 12 Turbine system subassembly.

the Pololu 25 mm diam gear motor is also cost efficient. While the cost of the system was not one of the primary design objectives for the prototyping stage, for this design to be practically implemented into existing guided air-drop systems, it must be able to be produced cost effectively. More information on the rotor and generator can be found in Sec. II.C.

For certain systems, such as bleed-air actuated systems, actuators and sensors are located inside the canopy rather than housed in the AGU. To transfer the generated power from the wind-energy-harvesting mechanism to these actuators and sensors, power lines can be run up along the rigging lines. For the short distance between the AGU and the canopy, approximately 10 m, a standard 22-gauge copper wire would have a total resistance of less than 1 mΩ, resulting in negligible power loss.

Initial wind tunnel testing suggested that the standard gear ratio of 9.68:1 increased the generator's load torque to a point at which the rotor could not spin near the predicted optimum tip-speed ratio, resulting in low overall efficiency. Therefore, a custom gear box was created to analyze several different gear ratios (Fig. 13). To fully optimize the system, the load impedance can be varied over a spectrum of gear ratios. The maximum efficiency for each gear ratio/impedance combination can be compared to determine the optimal
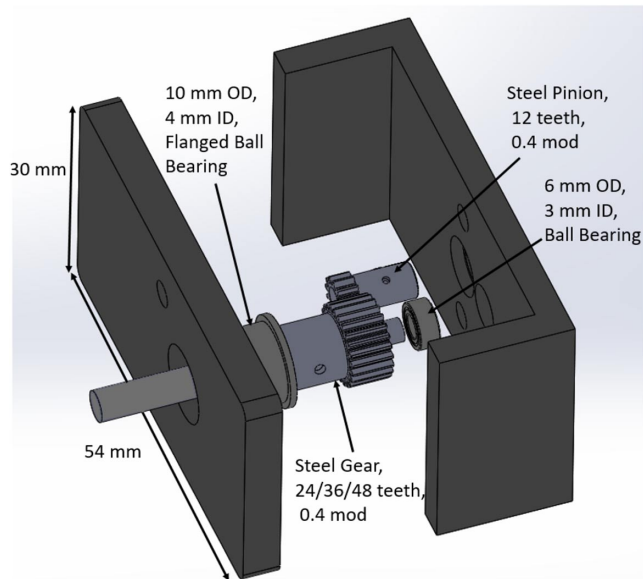
Fig. 13 2:1 ratio gear box, exploded view.

configuration. This Paper examines gear boxes with only one pinion–gear combination due to the large role that gear friction can play in small-scale energy-harvesting systems: each additional spur gear would only increase the system's total losses. Gear ratios of $2:1$, $3:1$, and $4:1$ were examined.

The shaft coupler was a custom, three-dimensional (3D)-printed part connecting the male output shaft of the motor to the female bore of the propeller. A set screw was used to maintain the connection between the motor shaft and the coupler, while the propeller hub and the coupler were epoxied together.

The housing was designed to minimize the projected area seen by the wind while maintaining structural integrity. The primary requirement for the housing was to maximize the protection of the energy-harvesting system in the event of a high-impact landing. Toward this end, the shroud diameter was designed to be approximately 0.5 in. larger than the rotor diameter. This was due to the rotor being suspended in a cantilever configuration; any significant impact force could cause the still-spinning rotors to deflect and contact the inner surface of the shroud. The impact could cause damage to the rotor blades, resulting in decreased performance on subsequent flights. Theoretically, the shroud could also be used as means of increasing aerodynamic efficiency. To maximize the added shroud efficiency, the shroud diameter should be designed to be slightly larger than the rotor, providing smoother airflow, increasing wind velocity, and minimizing tip losses.

To facilitate the experimental setup in the wind tunnel, eight eye screws were implanted into the inner portions of the housing, four on the top surface and four on the bottom. This was accomplished by press fitting threaded inserts into the 3D-printed parts and threading the eye screws into these features. As the top four eye screws needed to carry all the weight of the system, epoxy was added to enhance the strength of the press-fit connection between the threaded insert and the housing. The four screws on the bottom were used for stability purposes and will later serve to connect the AGU to the payload during flight.

IV. Wind Tunnel Test Results

A. Optimal Configuration Analysis

The power generated by the system at a given wind speed can be adjusted by matching the operating points of the aerodynamic and electrical subsystems. This section will focus on determining the optimum operating point of the system for three gear ratios by varying the output impedance.

1. Methodology

A series of tests was conducted to determine the optimal configuration of the system. Each of these experiments took place in the exhaust section of the low-turbulence wind tunnel at the Georgia Institute of Technology. The redesigned AGU was suspended from the roof of the wind tunnel using eye screws embedded in the top surface of the shroud and 500 lb parafoil chord. To improve rotational stability about the pitch axis, chord was tied from eye screws on the bottom surface of the shroud and attached to the floor of the test section. To mitigate unwanted yaw, the chord was threaded through gaps in between the outer upper and lower surfaces and tied off to the sides of the wind tunnel. The full experimental setup can be seen in Fig. 14.

To accurately measure power, an MSP432 microcontroller read voltage and angular velocity measurements every 0.5 s for 4 min. The voltage readings were measured using the analog to digital converter feature of the microcontroller and were passed through a low-pass filter with a cutoff frequency of 0.15 Hz. The generator was equipped with a 48 CPR quadrature encoder to provide the angular velocity measurements. The final 280 data points of the filtered voltage and angular velocity were averaged to find the nominal voltage and angular velocity for the specific test. Each test was conducted three times, and the average of the three tests was used as the final value. This process mitigated the effect of setup error on the measurements. Power generated was calculated using Eq. (9).

Each test was conducted in three stages: the preparation stage, the forward progression stage, and the reverse progression stage. The testing was divided into the forward and reverse progression stages to visualize any possible hysteresis in the system. During the preparation phase, the resistance value was tuned to within ± 0.5 Ω of the desired value, the AGU was tied firmly in place to ensure no unintentional movement occurred during the test, and the microcontroller was attached to the generator and encoder. The resistance values were determined in an iterative process beginning at 10 Ω and increasing until a clear trend became apparent.

The forward progression stage was designed to test the wind speeds in an increasing order, starting at 4.5 m/s and ramping up to 8 m/s. This range was selected to analyze conservative wind speeds for a lightweight parafoil-payload aircraft. The energy-harvesting system must be able to power the control and actuation systems even if it is only exposed to slower wind speeds during flight. The wind tunnel was activated, and the wind speed was manually set to 4.5 m/s by cross-referencing the pulse width modulation signal applied to the tunnel motor with the pitot tube attached to the test section.
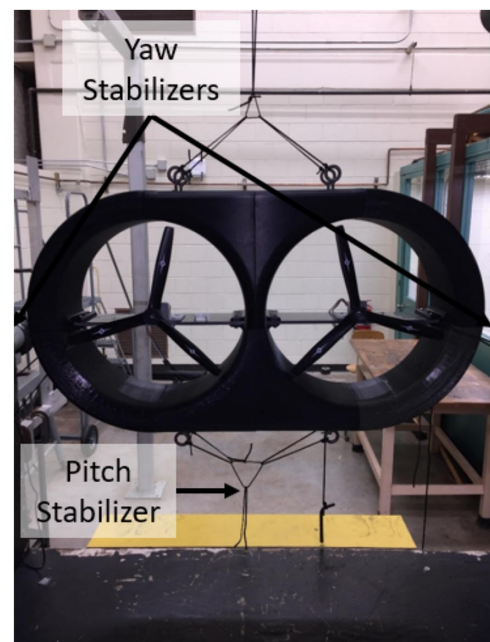

Fig. 14 Wind tunnel experimental setup.

Data collection began approximately 30 s after the wind tunnel speed was set. This allowed the turbine system to reach a steady state. Once the data had been recorded, the wind tunnel was set to the next highest speed in the test progression. The process was repeated until the 8 m/s case concluded.

Once the final test for the forward progression stage was complete, the reverse progression stage began. Without turning the wind tunnel off, the wind velocity was set from 8 to 7 m/s. The tests were conducted in a manner similar to the forward progression tests in which the turbine was allowed to reach a steady state and then data were recorded for 4 min. The next-lowest wind speed was then set, and the process was repeated until the 4.5 m/s case had been conducted. The wind tunnel was then turned off, and the preparation phase of the next test began.

2. Optimal Configuration Results

The overall efficiency of the system is a function of the tip-speed ratio of the rotor, the angular velocity of the generator, and the load impedance. The redesigned AGU was tested for a variety of load impedance values with 2∶1, 3∶1, and 4∶1 gear ratios. Power and angular velocity results from the 2∶1, 3∶1, and 4∶1 gear ratio configurations are shown in Figs. 15–20, in which the solid line represents the generated power of the configuration while the dashed line represents the angular velocity of the rotor. Error bars on all figures represent ±1 standard deviation.

The results from each gear ratio configuration show that the generated power increases with wind speed without exception. It is also clear that the load resistance plays an integral part in determining the efficiency of the system, particularly when the load resistance allows the generator speed to jump, or increase significantly with an increase in wind speed. This jump is a consequence of the torque characteristics of the Clark-Y airfoil employed by the rotor. Because of the jump phenomenon, substantial hysteresis was observed throughout testing. That is, a different amount of power was obtained when the wind tunnel speed was swept from low speed to high speed as compared to a sweep starting at a high speed and progressing to lower wind speeds. This is clearly visible contrasting the forward and reverse progression plots of Figs. 15–20. In all cases, the power generated in the reverse progression stage was greater than or approximately equal to the power generated in the forward progression stage. The physics behind the jump are further addressed in Sec. IV.A.3.

Figure 21 presents the most power-efficient impedance case for each gear ratio to clearly showcase the optimal configuration of the system. Designing for a specific case, 6 m/s, the 3∶1 gear ratio with 40 Ω load resistance is the most efficient, producing 1.73, 2.36, and 3.21 W at 6, 7, and 8 m/s, respectively. However, this is a conservative result. During flight, there was a certain amount of variability in airspeed due to the dynamic wind field. It is possible that the design point of 6 m/s could be exceeded to 8 m/s for sufficient time to induce the angular velocity jump. In this case, the optimum configuration of the system would be the 4∶1 gear ratio with 60 Ω load impedance, resulting in 1.06, 2.63, and 3.73 W at 6, 7, and 8 m/s wind speeds, respectively.

3. Analysis of Jump Phenomenon

As mentioned in Sec. IV.A.2, the jump phenomenon is a nonlinear dynamic response in which the measured generator speed, and thus generated power, increases significantly with an increase in wind speed. The observed hysteresis in the wind tunnel demonstrates that there are two stable equilibrium points in the system, a high-power producing and a low-power producing point, each one realizable depending on whether the wind speed progresses from low wind speeds to high wind speeds or from high wind speeds. This can be clearly seen in Fig. 22.

The drastic increase in rotor angular velocity noted during wind tunnel testing can be attributed to a sharp rise in the generated torque at a tip-speed ratio of approximately 1.5 (Fig. 8). When the wind
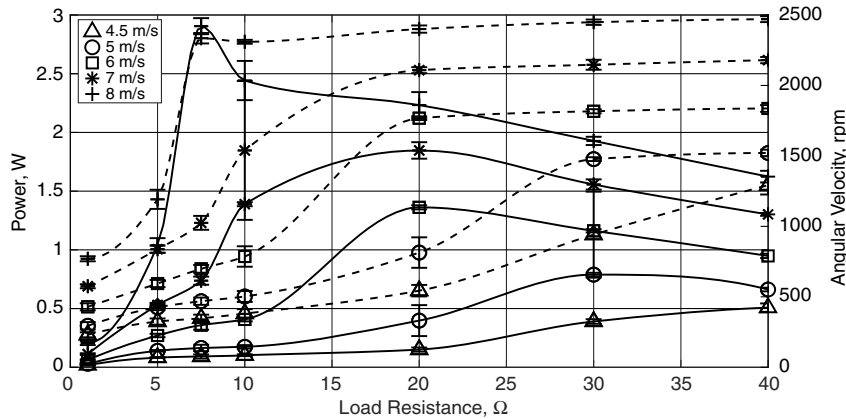

Fig. 15 Power and angular velocity vs load resistance for the 2∶1 gear ratio configuration, forward progression.
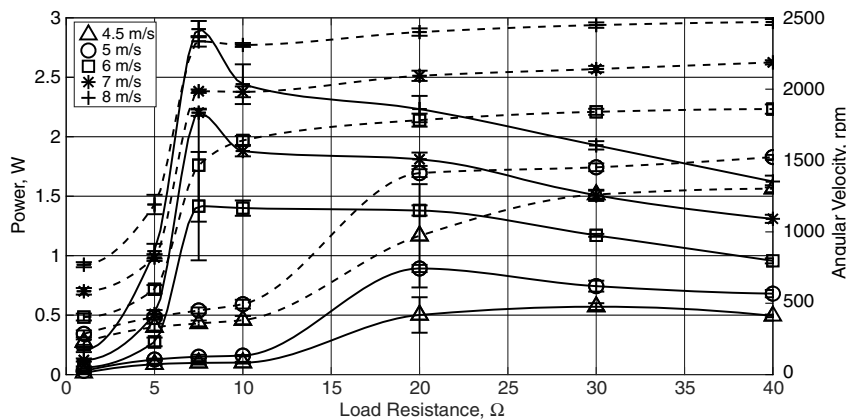

Fig. 16 Power and angular velocity vs load resistance for the 2∶1 gear ratio configuration, reverse progression.
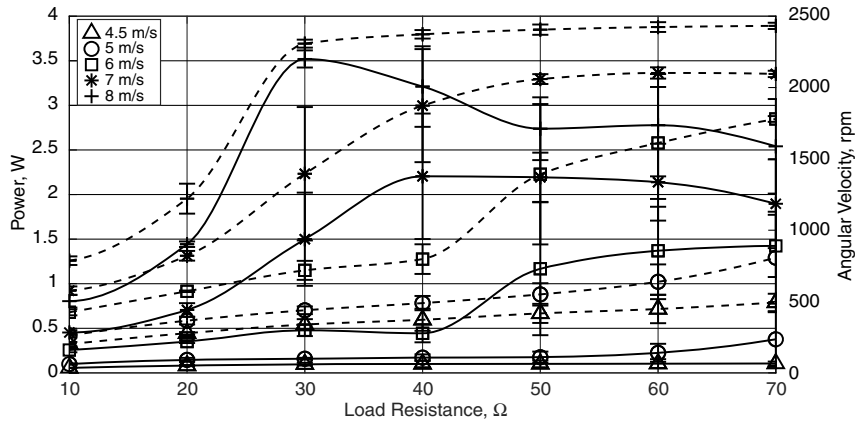
Fig. 17 Power and angular velocity vs load resistance for the 3∶1 gear ratio configuration, forward progression.
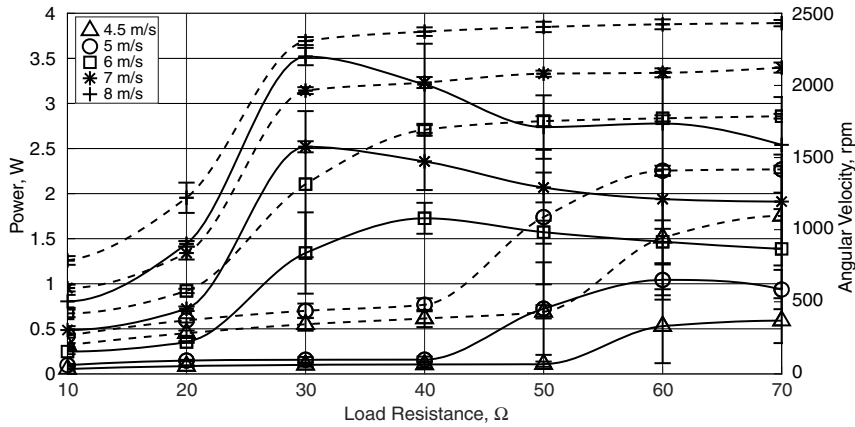
Fig. 18 Power and angular velocity vs load resistance for the 3∶1 gear ratio configuration, reverse progression.
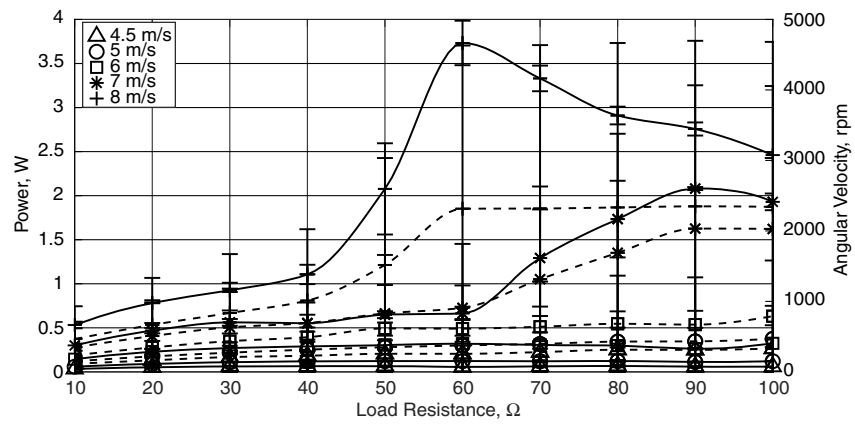
Fig. 19 Power and angular velocity vs load resistance for the 4∶1 gear ratio configuration, forward progression.
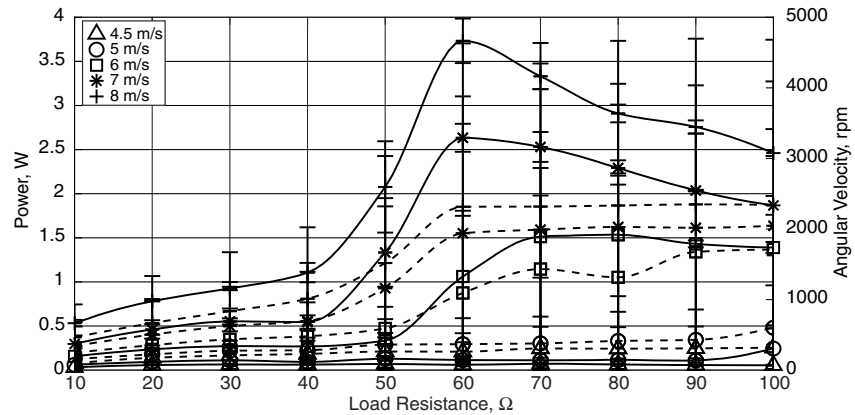
Fig. 20 Power and angular velocity vs load resistance for the 4∶1 gear ratio configuration, reverse progression.
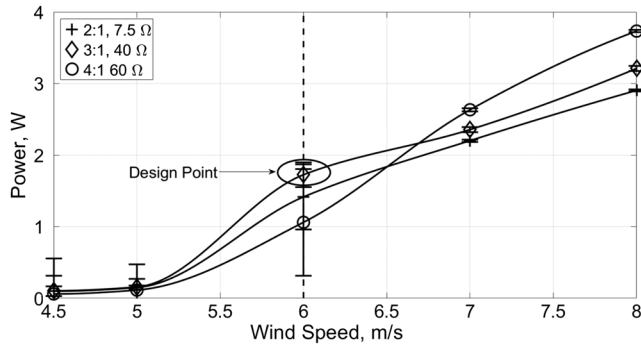
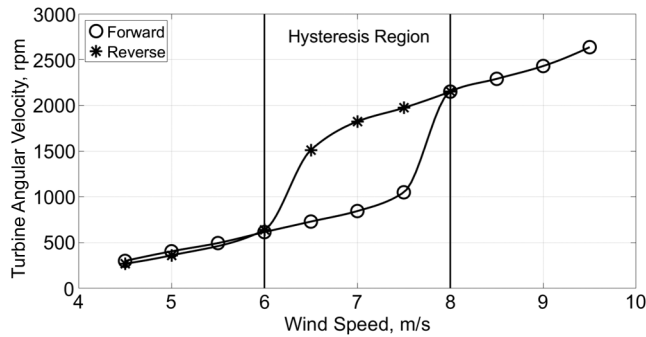**Fig. 21 Power vs wind speed for the optimal impedance cases of each gear ratio.**

Fig. 22 Experimentally observed hysteresis in the energy-harvesting system for the 4:1 gear ratio 50 Ω impedance configuration.

Fig. 23 Tip-speed ratio vs wind speed for the 4:1 gear ratio 50 Ω impedance configuration.

Fig. 24 Power variation vs angle of relative wind with a zero-order polynomial fit: a) Power vs side-slip angle and b) Power vs angle of attack.

speed was set to 4.5 m/s, the generated torque and the load torque reached a steady-state tip-speed ratio well below 1.5. As the wind speed progressed to higher speeds, the system generated more torque according to Fig. 8, yet the load torque continued to increase as well, causing the system to reach a steady state below the 1.5 tip-speed ratio threshold. At 8 m/s, the system reached a tip-speed ratio value of greater than 1.5. At this point, the generated torque increased more drastically than the load torque, which was mainly governed by viscous friction and back electromotive forces (EMFs) and thus was roughly proportional to angular velocity. The system accelerated over the maximum possible generated torque value at a tip-speed ratio of 3.0 and then began to generate less torque as the angular velocity got larger.

When the wind speed decreased from 8 to 7.5 m/s, the load torque naturally decreased with the reduced angular velocity. Immediately, the generated torque value decreased due to the system operating on a separate isowind speed line. This drop in generated torque caused the rotor to decelerate. However, while the rotor decelerated, the generated torque value increased, causing the load torque and the generated torque to equate before the maximum torque producing a tip-speed ratio value of 3.0. This trend continued until the decrease in wind speed caused the rotor to decelerate below a tip-speed ratio of 3.0. After this occurred, the rotor entered a positive feedback loop in which additional decreases in rotor angular velocity caused decreases in the generated torque. This continued until the generated torque and the load torque equated again, at the low-power equilibrium point. This is confirmed in the experimental results shown in Fig. 23.

B. Power Analysis at Nonoptimum Relative Angles

With the optimal configuration determined, the system must be examined under nonideal conditions, namely, different angles of relative wind. During flight, the AGU of the guided air-drop system will rarely have a zero-degree relative wind angle; nevertheless, the system must be able to provide sufficient power.

Tests were conducted to determine the effect of side-slip angle and angle of attack on power generation. The nonoptimum relative angle tests were directed in a manner similar to the optimal configuration
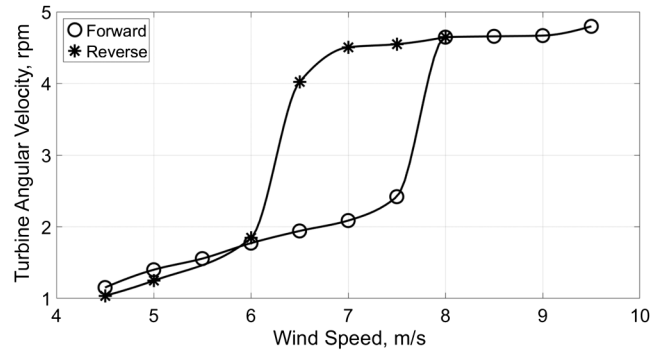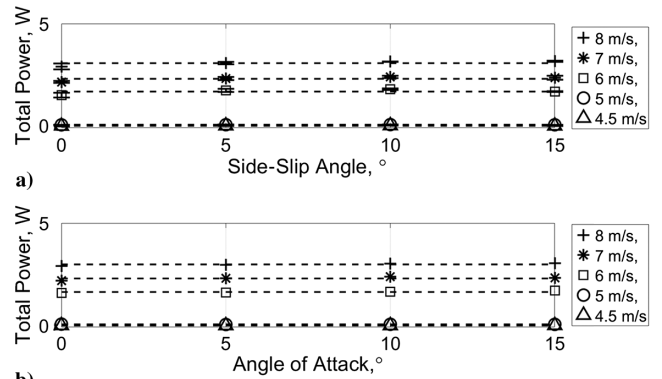
tests. Each test was conducted with a 3:1 gear ratio and a load impedance of 30 Ω.

Theoretically, for a nonducted, ideal rotor, the power should decrease by Eq. (11), in which P_N is the nominal power at a 0 deg angle of attack or side slip and α is the side-slip angle or angle of attack. Equation (11) is a product of the degradation of the effective rotor area by the cosine of the angle:

$$P = P_N \cos(\alpha) \tag{11}$$

In Fig. 24, plots of the power generated as a function of side slip and angle of attack are shown for constant wind speeds. Each marker represents a data point collected, while the dashed lines represent the best-fit constant. Again, the error bars on each data point represent ±1 standard deviation. The range of 0–15 deg was analyzed due to the limited range of the side-slip angle or angle of attack that an AGU experiences during flight. In fact, most dynamic models of parafoil-payload systems model the AGU as rigidly attached to the parafoil, highlighting the minimal relative wind angles an AGU typically experiences [22].

It is evident from Fig. 24 that the angle of side slip and the angle of attack had a minimal effect on generated power between 0 and 15 deg. The cosine of 15 deg is approximately 0.966. Reexamining Eq. (11), with a nonducted, ideal rotor, it would be expected that the power at the extreme angles would still be approximately 97% of the nominal power. This minimal difference is highlighted by the constant-value best-fit line. It should be noted that, while Fig. 24 only displays results for rotation in one direction, due to the design's symmetry, Fig. 24 will be symmetric about 0 deg of side slip and angle of attack.

V. Conclusions

A full-scale energy-harvesting system was successfully designed, fabricated, and tested in a wind tunnel. The results from the testing indicate that a modestly sized AGU with a rotor diameter of 0.33 m is able to provide over 3.7 W of power. According to data logged from a

typical bleed-air actuated flight, the average power required for controls and actuation was approximately 1.5 W. Even at the most conservative wind speeds, the wind turbine system was able to provide sufficient power to the system. In addition, it was determined that when operating at a nonoptimum relative wind angle, the power being produced from the turbine was not significantly diminished.

Furthermore, significant hysteresis in generated power was noted when the wind tunnel speed was swept from low speed to high speed as compared to starting at a high wind speed and progressing to lower speeds. This was determined to be caused by the torque characteristics of the airfoil employed by the rotor. The shape of the torque vs tip-speed ratio curve resulted in a drastic increase in generated torque for a modest increase in angular velocity. As the angular velocity did not significantly increase, the load torque, which was almost entirely dependent on viscous friction and back EMF, also did not significantly increase. The result was the rotor accelerated to a new, higher-power equilibrium point. These nonlinear dynamics can be leveraged to extract almost an order of magnitude more power from the system for certain configurations and wind speeds.

Acknowledgments

References

[1] George, S., Carter, D., Berland, J. C., Dunker, S., Tavan, S., and Barber, J., "The Dragonfly 4,500 kg Class Guided Airdrop System," *Infotech@Aerospace, Infotech@Aerospace Conferences*, AIAA Paper 2005-7095, Sept. 2005.
doi:10.2514/6.2005-7095

[2] Simpson, C., "Characteristics of Rechargeable Batteries," Tech. Rept. SNVA533, Texas Instruments, Dallas, TX, 2011.

[3] Hebert, C., Cowan, D., Peter, A., and Weiseman, C., "Aeroelastic Flutter," AIAA database, http://dl.btc.pl/kamami_wa/hk_24474_2.pdf [retrieved 1 March 2017].

[4] Ward, L., "Windbelt, Cheap Generator Alternative, Set to Power Third World," *Popular Mechanics*, Vol. 184, No. 9, Sept. 2015, pp. 72–80.

[5] Sivadas, V., and Wickenheiser, A. M., "A Study of Several Vortex-Induced Vibration Techniques for Piezoelectric Wind Energy Harvesting," *Proceedings of the SPIE 7977, Active and Passive Smart Structures and Integrated Systems 2011*, April 2011, Paper 79770F, https://doi.org/10.1117/12.878493.

[6] Lee, C., Liu, J., Liu, H., and Yang, B., *Micro and Nano Energy Harvesting Technologies*, 1st ed., Artech House, Boston, MA, 2015, pp. 204–209.

[7] Bae, J., Lee, J., Kim, S. M., Ha, J., Lee, B. S., Park, Y. J., Choong, C., Kim, J. B., Wang, Z. L., and Kim, H.-Y., et al., "Flutter-Driven Triboelectrification for Harvesting Wind Energy," *Nature Communications*, Vol. 5, No. 4929, Sept. 2014.
doi:10.1038/ncomms5929

[8] Federspiel, C. C., and Chen, J., "Air-Powered Sensor," *Proceedings of IEEE Sensors*, Vol. 1, Oct. 2003, pp. 22–25.
doi:10.1109/ICSENS.2003.1278888

[9] Rancourt, D., Tabesh, A., and Frechette, L., "Evaluation of Centimeter-Scale Micro Wind Mills: Aerodynamics and Electromagnetic Power Generation," *Proceedings of Power Microelectricalmechanical Systems*, Freiburg, Germany, Nov. 2007, pp. 93–96.

[10] Xu, F. J., Yuan, F. G., Hu, J. Z., and Qiu, Y. P., "Design of a Miniature Wind Turbine for Powering Wireless Sensors," *Proceedings of SPIE 7647, Sensors and Smart Structures Technologies for Civil, Mechanical, and Aerospace Systems 2010*, April 2010, Paper 764741, https://doi.org/10.1117/12.847429.

[11] Holmes, A. S., Hong, G., and Pullen, K. R., "Axial-Flux Permanent Magnet Machines for Micropower Generation," *Journal of Micro-electromechanical Systems*, Vol. 14, No. 1, 2005, pp. 54–62.
doi:10.1109/JMEMS.2004.839016

[12] Hirahara, H., Hossain, M. Z., Kawahashi, M., and Nonomura, Y., "Testing Basic Performance of a Very Small Wind Turbine Designed for Multi-Purposes," *Renewable Energy*, Vol. 30, No. 8, Jan. 2005, pp. 1279–1297.
doi:10.1016/j.renene.2004.10.009

[13] Priya, S., "Modeling of Electric Energy Harvesting Using Piezoelectric Windmill," *Applied Physics Letters*, Vol. 87, No. 18, Oct. 2005, pp. 1838–1844.
doi:10.1063/1.2119410

[14] Myers, R., Vickes, M., Kim, H., and Priya, S., "Small Scale Windmill," *Applied Physics Letters*, Vol. 90, No. 5, 2007.
doi:10.1063/1.2435346

[15] Carli, D., Brunelli, D., and Benini, L., "A High-Efficiency Wind-Flow Energy Harvester Using Micro Turbine," *2010 International Symposium on Power Electronics, Electrical Drives, Automation and Motion (SPEEDAM) 2010*, Pisa, Italy, June 2010, pp. 778–783.
doi:10.1109/SPEEDAM.2010.5542121

[16] Sardini, E., and Sprpelloni, M., "Self-Powered Wireless Sensor for Air Temperature and Velocity Measurements with Energy Harvesting Capability," *IEEE Transactions on Instrumentation and Measurement*, Vol. 60, No. 5, May 2011, pp. 1838–1844.
doi:10.1109/TIM.2010.2089090

[17] Danick, B., Yeatman, E., Roundy, S., Brand, O., Fedder, G. K., Hierold, C., Korvink, J. G., and Tabata, O., "Energy Harvesting from Fluid Flows," *Micro Energy Harvesting*, Wiley-Verlag Chemie, Weinheim, Germany, 2015, pp. 316–317.

[18] Huleihil, M., and Mazor, G., *Wind Turbine Power: The Betz Limit and Beyond*, 1st ed., Vol. 1, InTech Open Access, London, U.K., 2012, pp. 25–26.

[19] Scheuermann, E., Ward, M., Costello, M., Bergeron, K., and Noetscher, G., "Bleed Air Control: Towards the Complete In-Canopy System for Autonomous Aerial Delivery," *24th AIAA Aerodynamic Decelerator Systems Technology Conference*, AIAA Paper 2017-3883, 2017.

[20] Manwell, J. F., McGowan, J. G., and Rogers, A. L., "Aerodynamics of Wind Turbines," *Wind Energy Explained: Theory, Design and Application*, 2nd ed., Wiley, Hoboken, NJ, 2009, pp. 137–138.

[21] Miley, S. J., "A Catalog of Low Reynolds Number Airfoil Data for Wind Turbine Applications," Rept. RFP-3387, UC-60, U.S. Dept. of Energy, Wind Technology Division, Texas A&M Univ., College Station, TX, 1982.

[22] Slegers, N. J., "Comparison of Parafoil Dynamic Modes with Varying Payload Connections," *24th AIAA Aerodynamic Decelerator Systems Technology Conference, AIAA Aviation Forum*, AIAA Paper 2017-3878, June 2017.
doi:10.2514/6.2017-3878